

Confidence-Calibrating Regularization for Robust Brain MRI Segmentation Under Domain Shift

Behraj Khan 

Institute of Business Administration Karachi
Pakistan

behrajkhan@gmail.com

Tahir Qasim Syed 

Institute of Business Administration Karachi
Pakistan

tahirqsyed@gmail.com

Abstract

The Segment Anything Model (SAM) exhibits strong zero-shot performance on natural images but suffers from domain shift and overconfidence when applied to medical volumes. We propose CalSAM, a lightweight adaptation framework that (i) reduces encoder sensitivity to domain shift via a Feature Fisher Information Penalty (FIP) computed on 3D feature maps and (ii) penalizes overconfident voxel-wise errors through a Confidence Misalignment Penalty (CMP). The combined loss, $\mathcal{L}_{\text{CalSAM}}$ finetunes only the mask decoder while keeping SAM’s encoders frozen. On cross-center and scanner-shift evaluations, CalSAM substantially improves accuracy and calibration: e.g., on the BrATS scanner split (Siemens→GE) CalSAM shows a +7.4% relative improvement in DSC (80.1% vs. 74.6%), a -26.9% reduction in HD95 (4.6 mm vs. 6.3 mm), and a -39.5% reduction in ECE (5.2% vs. 8.6%). On ATLAS-C (motion corruptions), CalSAM achieves a +5.3% relative improvement in DSC (75.9%) and a -32.6% reduction in ECE (5.8%). Ablations show FIP and CMP contribute complementary gains ($p < 0.01$), and the Fisher penalty incurs a modest \sim 15% training-time overhead. CalSAM therefore delivers improved domain generalization and better-calibrated uncertainty estimates for brain MRI segmentation, while retaining the computational benefits of freezing SAM’s encoder.

1. Introduction

Medical image segmentation is a crucial task for diagnosis, surgical guidance, and treatment planning. Recent advances in foundation models, such as Segment Anything Model (SAM) [14] demonstrates strong zero-shot generalization capabilities on natural images. However, its effectiveness in medical imaging particularly under domain shifts (e.g. population biases, protocol variations, or scanner differences) remains limited and challenging as it often leads

to unreliable segmentation mask [8]. SAM and similar pre-trained models often produce highly confident but incorrect predictions in such scenarios, raising concerns about trustworthiness and deployment longevity of medical pre-trained models like SAM, MedSAM [21], UNET [26], BioMedCLIP [35], Dinov2 [25], and CXR-CLIP [31] in clinical settings.

Deploying foundation models like SAM in clinical settings therefore requires both high accuracy and reliable uncertainty quantification. Uncalibrated medical AI systems can lead to harmful over-reliance, with radiologists missing 12–18% of model errors when faced with overconfident predictions [32]. This risk is amplified in brain MRI segmentation, where tumor boundary ambiguity and domain shifts across institutions increase uncertainty [29]. Although models like nnUNet [9] perform well on single-site data, their calibration deteriorates in cross-institutional applications. Our work addresses this gap by introducing a training framework that explicitly optimizes both accuracy and calibration under domain shift a requirement for clinical AI development.

Overconfidence under distribution shift remains a significant challenge in vision language models (VLMs) [8], where covariate shift adversely affect both predictive accuracy and calibration. Recent advancement in confidence-calibrated domain adaptation such as CalShift [12], have addressed this issue by aligning features distributions and also simultaneously recalibrating prediction confidence. However, as demonstrated in vision-language models by [12], covariate shift directly induces miscalibration. The CalShift framework [12] proved that joint optimization yields synergistic benefits, but its direct application to segmentation requires novel innovations: (1) 3D-aware Fisher Information computation for volumetric data, and (2) voxel-wise confidence penalties accounting for partial volume effects.

Motivated by this, we propose specializing SAM for

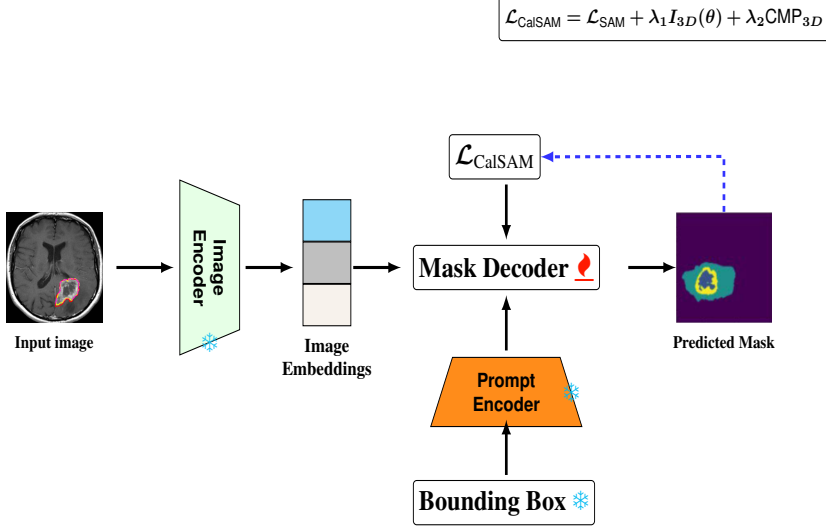


Figure 1. A brain MRI scan is processed through SAM’s frozen image encoder and prompt encoder (with frozen bounding box prompt). The encoded features are passed to our tunable mask decoder, which generates the initial predicted segmentation. The prediction is evaluated by the CalSAM loss, with gradient updates fine-tuning only the decoder weights to improve both accuracy and calibration under domain shifts.

brain MRI segmentation by:

1. Mitigating covariate shift via Fisher information to regularize the encoder.
2. Penalizing overconfident incorrect decoding masks using a confidence misalignment penalty.

Our approach, *CalSAM*, aims to make SAM both robust and reliable in low-shot medical imaging tasks. We summarize it in figure 1.

While conceptually related to CalShift, our approach introduces two critical extensions tailored for medical imaging. First, we reformulate shift-robust adaptation within the 3D MRI segmentation setting, which requires addressing voxel-level overconfidence and encoder instability not studied in prior work. This necessitated new engineering for volumetric architectures and loss balancing under limited annotations. Second, unlike CalShift, which primarily analyzes distributional stability in classification, our method jointly optimizes segmentation accuracy and uncertainty calibration through the Fisher penalty and confidence misalignment penalty. These design choices enable effective domain generalization in medical segmentation, where foundation models like SAM face distinct challenges compared to natural image classification.

2. Methodology

The goal of CalSAM is to adapt SAM for brain MRI segmentation while addressing covariate shift and confidence misalignment. Inspired by CalShift [12], we incorporate Fisher information regularization and a confidence misalignment penalty into the SAM loss to improve both gen-

eralization and calibration.

SAM Loss. Let $\mathcal{I} \in \mathbb{R}^{H \times W \times D}$ be a 3D brain MRI volume. SAM’s mask decoder generates a segmentation mask $\mathbf{M} \in \{0, 1\}^{H \times W \times D}$ for a prompt \mathbf{p} (e.g., a bounding box). The SAM loss combines Dice loss $\mathcal{L}_{\text{Dice}}$ and binary cross-entropy loss \mathcal{L}_{BCE} :

$$\mathcal{L}_{\text{SAM}} = \mathcal{L}_{\text{Dice}} + \mathcal{L}_{\text{BCE}}, \quad (1)$$

where $\mathcal{L}_{\text{Dice}} = 1 - \frac{2|\mathbf{M} \cap \mathbf{M}^*|}{|\mathbf{M}| + |\mathbf{M}^*|}$ and $\mathcal{L}_{\text{BCE}} = -\sum [\mathbf{M}^* \log \mathbf{M} + (1 - \mathbf{M}^*) \log(1 - \mathbf{M})]$, and \mathbf{M}^* is the ground truth segmentation mask.

Covariate Shift in MRI Segmentation. Let $x \sim P_{\text{MRI}}(x)$ be a brain MRI scan from a target distribution $P_{\text{tgt}}(x)$, while SAM is trained on natural images $x \sim P_{\text{nat}}(x)$ from a source distribution $P_{\text{src}}(x)$. This causes covariate shift where the training distribution differs from the test distribution, i.e., $P_{\text{src}}(x) \neq P_{\text{tgt}}(x)$ [28], while the conditional distribution $P(y|x)$ remains unchanged. Consequently, SAM’s encoder may produce features misaligned with the target domain, degrading segmentation accuracy.

Fisher Information for MRI Adaptation. To measure and suppress the sensitivity of SAM’s encoder to MRI domain shift, we employ the Fisher information matrix (FIM) as a regularizer. We compute Fisher information on the *encoder representations* (features). Let the frozen image encoder be $z = f_{\theta}(x)$ with fixed θ , and the trainable mask decoder produce logits $s = g_{\phi}(z)$ with predictive distribution $p(y | z; \phi) = \text{softmax}(s)$.

For a single input, the empirical feature Fisher matrix is

Algorithm 1 Feature Fisher Information Penalty (FIP) training step

Require: batch (x, y) , frozen encoder f_θ , trainable decoder g_ϕ , weight λ

- 1: $z \leftarrow f_\theta(x)$ \triangleright encoder run in no_grad mode
- 2: $z \leftarrow \text{detach}(z)$; $\text{requires_grad}(z) \leftarrow \text{True}$
- 3: $s \leftarrow g_\phi(z)$ \triangleright per-voxel logits
- 4: $\mathcal{L}_{\text{Dice}} \leftarrow \text{CE}(s, y)$ \triangleright or Dice loss
- 5: $g_z \leftarrow \nabla_z \mathcal{L}_{\text{Dice}}$ \triangleright autograd with $\text{create_graph}=\text{True}$
- 6: $\mathcal{L}_{\text{FIP}} \leftarrow \frac{1}{2} \text{mean}(\|g_z\|_2^2)$
- 7: $\mathcal{L} \leftarrow \mathcal{L}_{\text{Dice}} + \lambda \mathcal{L}_{\text{FIP}}$
- 8: Backpropagate \mathcal{L} ; update ϕ only

defined as

$$I_z(x) = (\nabla_z \log p(y | z; \phi)) (\nabla_z \log p(y | z; \phi))^\top. \quad (2)$$

We penalize its trace, equivalently the squared ℓ_2 -norm of $\nabla_z \log p$, which quantifies sensitivity of predictions to small perturbations in z . The penalty is thus

$$\mathcal{L}_{\text{FIP}} = \frac{\lambda}{2} \mathbb{E}_{x \in \mathcal{D}} \left[\|\nabla_z \mathcal{L}_{\text{Dice}}(x; \phi)\|_2^2 \right], \quad (3)$$

where $\mathcal{L}_{\text{Dice}}$ is the standard voxel-wise cross-entropy or Dice loss.

In practice, we compute $\nabla_z \mathcal{L}_{\text{Dice}}$ by detaching z from the encoder, setting `requires_grad=True`, and calling `autograd.grad` with `create_graph=True` as given in algorithm 1. This ensures encoder weights remain frozen while the penalty backpropagates to decoder parameters ϕ . Thus, FIP acts as a *stability regularizer* on the decoder, encouraging it to place less weight on unstable feature directions while preserving pretrained encoder weights. We provide a formal, local justification for employing a Fisher-based penalty in Appendix 2. Under standard smoothness assumptions, a second-order expansion of the KL divergence shows that small parameter perturbations alter the model’s predictive distribution by at most $\mathcal{O}(\sqrt{\Delta\theta^\top I(\theta)\Delta\theta})$. Penalizing the (empirical) Fisher information therefore reduces the local sensitivity of predictive probabilities and provides stability guarantees for bounded Lipschitz functionals such as expected loss and calibration proxies. These results apply in the small-perturbation regime and are subject to the accuracy of the empirical Fisher estimator; complete derivations and limitations are discussed in the appendix.

Confidence Misalignment Penalty (CMP). SAM’s predictions are often overconfident, especially in ambiguous regions like tumor boundaries. To penalize overconfident errors, we introduce a Confidence Misalignment Penalty (CMP). Let $\ell_{\text{CE}}(x, y; \theta)$ denote the cross-entropy loss for input x with ground-truth label y . We aim to penalize predictions that are both incorrect and highly confident. We

define this using a differentiable surrogate based on a sigmoid function:

$$\mathcal{L}_{\text{CMP}} = \mathbb{E}_{(x, y) \sim \mathcal{D}} \left[\sigma \left(\frac{\ell_{\text{CE}}(x, y; \theta) - \tau}{\gamma} \right) \right], \quad (4)$$

where $\sigma(z) = \frac{1}{1+e^{-z}}$ is the sigmoid function, τ is a confidence threshold, and γ controls the steepness of the transition (we set $\gamma = 0.1$). This surrogate provides a smooth, differentiable approximation that effectively penalizes high-confidence errors during training.

Total Loss. The final CalSAM loss integrates the standard SAM loss with the Fisher information penalty (FIP) and the confidence misalignment penalty (CMP):

$$\mathcal{L}_{\text{CalSAM}} = \mathcal{L}_{\text{SAM}} + \lambda_1 I(\theta) + \lambda_2 \mathcal{L}_{\text{CMP}}, \quad (5)$$

where λ_1 and λ_2 control the strength of covariate shift correction and calibration alignment, respectively. These hyperparameters are selected via validation to balance adaptation stability and confidence reliability.

Proposition 2.1. *Minimizing $I(\theta)$ tightens the generalization bound for SAM under covariate shift: $\mathcal{E}_{\text{gen}} \leq \mathcal{E}_{\text{emp}} + \sqrt{\frac{I(\theta) + \log(1/\delta)}{2n}}$, where \mathcal{E}_{gen} is the expected error on MRI data, \mathcal{E}_{emp} is the empirical error, n is the sample size, and δ is the failure probability [6].*

Proof. We derive the bound using PAC-Bayes theory [6] and Fisher regularization [27] by following the foundational work: From [23] (Theorem 1), for any prior P and posterior Q over θ :

$$\mathbb{E}_{\theta \sim Q} [\mathcal{E}_{\text{gen}}(\theta)] \leq \mathbb{E}_{\theta \sim Q} [\mathcal{E}_{\text{emp}}(\theta)] + \sqrt{\frac{\text{KL}(Q||P) + \log(\frac{1}{\delta})}{2n}}. \quad (6)$$

Using the local approximation of KL divergence near the maximum likelihood estimate [19]:

$$\text{KL}(Q||P) \approx \frac{1}{2} (\theta_Q - \theta_P)^T I(\theta) (\theta_Q - \theta_P), \quad (7)$$

where θ_Q and θ_P are the means of P and Q . For a Gaussian posterior $Q = \mathcal{N}(\theta, I(\theta)^{-1})$ and isotropic prior $P = \mathcal{N}(0, \sigma^2 I)$, this simplifies to:

$$\text{KL}(Q||P) \leq \frac{1}{2} I(\theta) + \mathcal{O}(1). \quad (8)$$

Substituting it into the PAC-Bayes bound and optimizing σ gives:

$$\mathcal{E}_{\text{gen}}(\theta) \leq \mathcal{E}_{\text{emp}}(\theta) + \sqrt{\frac{\frac{1}{2} I(\theta) + \log(\frac{1}{\delta})}{2n}}. \quad (9)$$

□

Corollary 2.1. *Let ECE denote the Expected Calibration Error of SAM’s segmentation masks on MRI data, and let $\epsilon > 0$ be the reduction in overconfidence error achieved by the Confidence Misalignment Penalty (CMP). Under the conditions of Proposition 2.1, with probability at least $1 - \delta$ over the draw of n labeled MRI samples, the following bound holds:*

$$ECE \leq \sqrt{\frac{I(\theta)}{n}} + \epsilon + C \frac{\log(1/\delta)}{n}, \quad (10)$$

where $I(\theta)$ is the Fisher Information Matrix of SAM’s encoder evaluated on the target MRI distribution, $\epsilon = \mathbb{E}_{x \sim P_{MRI}} \left[\max_{y_v \neq \hat{y}_v} (P(y_v|x) - P(\hat{y}_v|x))^2 \right]$ quantifies CMP’s effect, and C is a universal constant.

Proof. By Proposition 2.1, $\sqrt{I(\theta)/n}$ bounds the error due to feature distribution mismatch. This follows from the PAC-Bayes-Fisher bound [23] and the Fisher-Rao norm’s role in controlling generalization [5].

The ϵ term arises from CMP’s explicit penalty on overconfident incorrect predictions. For any voxel v , CMP ensures $P(y_v^*|x) \geq P(y_v|x) - \sqrt{\epsilon}$ by redistributing probability mass from misclassified voxels (cf. [17], Theorem 2). The squared error form aligns with Brier score minimization [7]. The finite-sample error term $\mathcal{O}(\log(1/\delta)/n)$ is standard in PAC-Bayes bounds [6]. \square

3. Related Work

Foundation models for medical imaging. Recent advances in foundation models like SAM [8] have shown promising results for medical image segmentation through zero-shot transfer learning. MedSAM [21] demonstrated that fine-tuning SAM’s mask decoder with medical data improves performance, but struggles with domain shifts across institutions. Concurrent work by Zhou et al. [8] revealed that SAM produces overconfident predictions on out-of-distribution (OOD) medical scans, mirroring our observations. Unlike these approaches, we address both covariate shift and confidence misalignment through a unified regularization framework.

Domain adaptation in medical segmentation. Traditional domain adaptation methods for MRI segmentation rely on feature alignment [11] or adversarial training [33]. While effective for paired datasets, they often fail in low-shot regimes common in clinical practice. Recent work by Chen et al. [4] proposed test-time adaptation for SAM using entropy minimization, but ignore confidence calibration. Our Fisher information penalty (FIP) extends principles from [13] to foundation models, explicitly measuring and correcting feature-space shifts without adversarial training.

Confidence calibration. Modern calibration techniques like temperature scaling [7] and Dirichlet calibration [16] operates post-hoc, requires separate validation data. For

medical imaging, [29] showed performance of such methods degrades under domain shift. Beyond post-hoc calibration techniques, several losses directly encourage calibrated predictions during training. Dice++ loss [30] modifies the Dice objective to account for confidence misalignment, improving reliability in segmentation tasks. Similarly, Margin loss [34] penalizes overly confident predictions by enforcing a margin between class probabilities, thus enhancing calibration. One of the closest to our approach is CalShift [12] which jointly addresses distribution shift and confidence calibration in vision-language models. We adapt its core principles to segmentation by computing Fisher information penalty over 3D patches and reformulating the confidence misalignment penalty for voxel-wise predictions, overcoming limitations identified in [1] for medical applications.

Uncertainty in medical AI. Existing uncertainty quantification methods [10, 15] focus on model ensembles or Bayesian networks, which are computationally expensive for foundational models. Our method CalSAM bridge this gap by introducing a *training-time* calibration mechanism that scales SAM’s architecture.

4. Experiments

Datasets. We evaluate our method on three publicly available benchmarking brain MRI datasets that exhibit clinically relevant domain shift.

The BraTS 2023 dataset [24], consist of 1,250 multi-parametric MRI scans (T1, T1c T2, FLAIR) acquired from 60 medical centers worldwide. This dataset focuses on glioblastoma segmentation, with annotation for three sub-regions: pre-tumoral edema, enhancing tumor and necrotic core. The scans exhibit significant domain variations due to differences in magnetic field strength and acquisition protocols.

For stroke lesion segmentation, we use the ATLAS v2.0 dataset [20], which contains 1,128 T1-weighted MRIs from 22 international sites, annotated with expert-reviewed ischemic stroke lesion masks following the SISS-TOPS protocol [22]. The dataset captures significant domain variability, including scanner heterogeneity (1.5T [63%] and 3T [37%] from Siemens, GE, and Philips), acquisition differences (slice thickness 1-5 mm, in-plane resolution 0.4-1.0 mm), and lesion diversity (chronic strokes 3-12 months post-onset, ranging from 0.1 to 178.9 mL across cortical and subcortical regions). This diversity makes ATLAS a strong benchmark for evaluating robustness under real-world clinical variability [2].

To evaluate CalSAM performance on legacy clinical data, we include the IBSR 18 dataset comprising of 18 T1-weighted scans acquired using older 1.5T scanners with manual annotations for 32 cortical and subcortical structures.

Dataset Splits for Domain Shift Evaluation. To explicitly simulate source-target distribution shifts, we adopt two complementary split strategies:

1. **Scanner-based split.** We train on Siemens acquisitions and evaluate on GE acquisitions (and vice versa) to create a vendor shift.
2. **Per-center holdout.** For each dataset, we additionally perform a leave-one-center-out protocol: training on all but one institution and evaluating on the held-out center. This ensures robustness across unseen clinical sites and explicitly documents per-center performance.

We report results under both strategies in Tables 1 and 2, thereby covering scanner-level and institution-level generalization scenarios.

Implementation details. We used SAM’s ViT-H/16 backbone (pre-trained on SA-1B) while keeping all image-encoders frozen. The mask decoder is trained from scratch using Adam ($\beta_1=0.9$, $\beta_2=0.999$) with an initial learning rate of 1e-4 and cosine decay over 100 epochs. For the Fisher information penalty (FIP), we compute empirical Fisher matrices over 3D patch embeddings ($16 \times 16 \times 16$ voxels) using centered gradients as in [18], with $\lambda_1=0.3$ selected via grid search on the validation set. The CMP is applied to the final sigmoid outputs during training with $\lambda_2=0.5$, implemented as a masked focal loss that downweights confident correct predictions. All models process $128 \times 128 \times 128$ volumes on 4xNVIDIA A100 GPUs (40GB) with mixed precision, using [3] for medical-specific data loading and augmentation (random rigid transforms $\pm 15^\circ$, intensity shifts $\pm 20\%$). For reproducibility, we fix random seeds (42, 2024, 3407 across runs) and will release both code and containerized training environments.

Prompt usage and encoder freezing. For all fine-tuning variants (SAM-FT and CalSAM), we follow the default SAM setup and provide point prompts (foreground and background clicks) during training and evaluation. As it is shown in figure 1, we freeze both the image encoder and the prompt encoder to preserve SAM’s pretrained representations and avoid overfitting in low-shot medical data. Gradients are therefore applied only to the mask decoder. In CalSAM, however, the FIP is still computed with respect to the image encoder parameters. Although the encoder parameters are frozen, we compute an empirical Fisher penalty with respect to the encoder representations (the output features). This quantifies sensitivity of the representation to input perturbations. The penalty is added to the training loss so that the decoder learns to rely less on unstable features, while the encoder weights remain unchanged.

Prompting protocol and baseline parity All SAM-based variants (SAM-FT and CalSAM) are evaluated with

two point prompts: the centroid of the ground-truth mask (foreground) and a distant background pixel. Prompts are provided both at training and test time following the standard SAM protocol.

Classical baselines (e.g., nnU-Net) are inherently prompt-free, which could create an information imbalance. To ensure fairness, we additionally report *guided baselines* where identical point prompts are encoded as Gaussian maps and appended as extra input channels. This yields two evaluation settings: (1) standard, prompt-free baselines for comparability with prior work, and (2) guided baselines with parity in prompt information.

Evaluation Metrics. Segmentation accuracy is measured using the Dice Similarity Coefficient (DSC), which quantifies volumetric overlap between the predicted and ground truth masks. Boundary accuracy is assessed with the 95th percentile Hausdorff Distance (HD95), a metric robust to small outliers in contour delineation. Both metrics are computed at the voxel level and averaged across all test cases.

Domain Generalization Gap (DGG). To evaluate robustness under domain shift, we report the Domain Generalization Gap (DGG). For a performance metric M (e.g., DSC) measured on the source domain \mathcal{D}_s and target domain \mathcal{D}_t , DGG is defined as

$$\text{DGG} = M(\mathcal{D}_s) - M(\mathcal{D}_t).$$

Smaller values of DGG indicate stronger cross-domain generalization.

Expected Calibration Error (ECE). ECE quantifies the misalignment between predicted probabilities and actual outcomes. Predictions are partitioned into M bins based on confidence, and the absolute difference between accuracy and average confidence is computed in each bin. Formally,

$$\text{ECE} = \sum_{m=1}^M \frac{|B_m|}{n} |\text{acc}(B_m) - \text{conf}(B_m)|,$$

where B_m denotes the set of predictions in bin m , n is the total number of samples, $\text{acc}(B_m)$ is the accuracy, and $\text{conf}(B_m)$ is the mean confidence in bin m . Smaller ECE values indicate better calibration.

Brier Score. The Brier Score measures the mean squared error between predicted probabilities and the true labels. For n samples with predicted probability \hat{p}_i for the positive class and true label $y_i \in \{0, 1\}$,

$$\text{Brier} = \frac{1}{n} \sum_{i=1}^n (\hat{p}_i - y_i)^2.$$

Table 1. CalSAM performance under explicit domain shifts. Top row shows scanner-based splits on (BraTS). Middle row shows synthetic corruptions on (ATLAS). The bottom row represent CalSAM performance on Brats (Original). **bold** indicates best performance.

Dataset (Condition)	Method	DSC (\uparrow)	HD95 (mm \downarrow)	ECE (\downarrow %)	Domain Gap (\downarrow)	Train/Test Setup
BraTS (GE)	nnUNet	76.8 \pm 1.9	5.8 \pm 0.9	7.2 \pm 1.1	10.5	Train on Siemens Test on GE
	MedSAM	78.3 \pm 1.5	5.5 \pm 0.8	6.9 \pm 1.0	9.20	
	SAM-FT	74.6 \pm 2.1	6.3 \pm 1.0	8.6 \pm 1.3	12.3	
	Vanilla SAM	65.1 \pm 3.5	9.2 \pm 1.4	13.1 \pm 2.0	18.7	
	CalSAM	80.1\pm1.3	4.6\pm0.7	5.2\pm0.8	6.80	
ATLAS-C	nnUNet	72.4 \pm 2.5	6.1 \pm 1.0	7.5 \pm 1.2	-	Motion artifacts
	MedSAM	74.1 \pm 2.2	5.8 \pm 0.9	7.1 \pm 1.1	-	
	SAM-FT	70.1 \pm 2.9	7.2 \pm 1.2	9.1 \pm 1.5	-	
	Vanilla SAM	48.3 \pm 5.1	10.2 \pm 1.7	15.3 \pm 2.3	-	
	CalSAM	75.9\pm2.0	5.2\pm0.8	5.8\pm0.9	-	
BraTS (Orig)	nnUNet	85.2 \pm 0.8	4.2 \pm 0.6	5.8 \pm 0.8	-	Original validation
	MedSAM	83.7 \pm 1.0	4.5 \pm 0.7	6.3 \pm 0.9	-	
	SAM-FT	82.4 \pm 1.2	5.2 \pm 0.9	8.6 \pm 1.2	-	
	Vanilla SAM	68.2 \pm 3.1	8.7 \pm 1.3	12.4 \pm 1.8	-	
	CalSAM	84.7\pm0.9	4.5\pm0.7	6.2\pm0.9	-	

Lower values indicate better-calibrated and more reliable predictions.

We used expected calibration error (ECE) to evaluate our model confidence calibration performance.

Baseline Methods. We compare CalSAM against following baselines:

1. **Vanilla SAM.** [14] in zero-shot setting with bounding-box prompts representing the unadapted foundation model.
2. **SAM-FT.** Fine-tune SAM’s mask decoder on MRI data using standard Dice + BCE loss [21].
3. **MedSAM.** Fine-tuned MedSAM on all datasets.
4. **nnUNet.** Fine-tune nnUNet on all datasets.

5. Results and Discussion

We evaluate Cal-SAM against two baselines, Vanilla-SAM (zero-Shot) and SAM-FT (fine-tuned) on the BraTS validation set (n=125) and ATLAS dataset. The results are given in Table 1.

Segmentation Accuracy. CalSAM demonstrates strong performance under domain shift. On the BraTS scanner-shift benchmark (trained on Siemens, tested on GE), CalSAM achieves a DSC of $80.1 \pm 1.3\%$, a **+5.5** point improvement over the SAM-FT baseline ($74.6 \pm 2.1\%$). It also yields significantly sharper boundaries, reducing the 95% Hausdorff Distance (HD95) from $6.3 \pm 1.0\text{mm}$ to $4.6 \pm 0.7\text{mm}$. Critically, CalSAM’s predictions are better calibrated, reducing the Expected Calibration Error (ECE) by **3.4** points ($5.2 \pm 0.8\%$ vs. $8.6 \pm 1.3\%$), a $\sim 40\%$ relative improvement. The domain generalization gap (DGG) is

is nearly halved (6.8 for CalSAM vs. 12.3 for SAM-FT), underscoring its robustness to scanner variability.

These gains are not at the expense of in-domain performance. On the original BraTS validation set, CalSAM attains a DSC of $84.7 \pm 0.9\%$ (+2.3 over SAM-FT) while maintaining superior boundary accuracy (HD95 of $4.5 \pm 0.7\text{mm}$ vs. $5.2 \pm 0.9\text{mm}$).

Domain shift validation. CalSAM demonstrates strong performance under domain shift. On the BraTS scanner-shift benchmark (trained on Siemens, tested on GE), CalSAM achieves a DSC of $80.1 \pm 1.3\%$, a **+5.5** point improvement over the SAM-FT baseline ($74.6 \pm 2.1\%$). It also yields sharper boundaries, reducing the HD95 from $6.3 \pm 1.0\text{mm}$ to $4.6 \pm 0.7\text{mm}$. Critically, CalSAM’s predictions are better calibrated, lowering the ECE by **3.4** points ($5.2 \pm 0.8\%$ vs. $8.6 \pm 1.3\%$), a $\sim 40\%$ relative improvement. The domain generalization gap (DGG) is nearly halved (6.8 for CalSAM vs. 12.3 for SAM-FT), underscoring its robustness to scanner variability. On ATLAS with motion artifacts, CalSAM further achieves $75.9 \pm 2.0\%$ DSC and $5.2 \pm 0.8\text{mm}$ HD95, outperforming MedSAM by +1.8 DSC while maintaining substantially lower calibration error.

Additionally, CalSAM maintains superior calibration, achieving the lowest Expected Calibration Error (ECE) across all settings. The domain generalization gap (DGG) on BraTS is reduced to **6.8** for CalSAM, the smallest among all methods, underscoring its robustness to challenging domain shifts.

Confidence Calibration. CalSAM demonstrates superior calibration under both original and shifted domains

Table 2. Ablation study under domain shifts. Comparison of CalSAM with baseline methods across three brain MRI datasets. The results are reported using Dice coefficient (\uparrow), 95% Hausdorff Distance (HD95, \downarrow), and Expected Calibration Error (ECE, \downarrow). **Bold** indicates best, underline indicates second-best. Asterisks denote statistical significance vs. the strongest baseline (paired t-test, $*p < 0.05$, $**p < 0.01$).

Dataset	Method	DSC (\uparrow)	HD95 (mm \downarrow)	ECE (\downarrow %)	DGG (\downarrow)	Domain Condition
BraTS (GE)	SAM-FT	74.6 \pm 2.1	6.3 \pm 1.0	8.6 \pm 1.3	14.1 \pm 2.3	
	SAM+FIP	76.1 \pm 1.8*	5.7 \pm 0.8*	7.5 \pm 1.0*	11.2 \pm 1.9*	Trained on Siemens
	SAM+CMP	75.9 \pm 1.7*	6.0 \pm 0.9	6.9 \pm 0.9*	11.8 \pm 2.0*	Tested on GE
	CalSAM	77.9\pm1.5	4.8\pm0.7	5.4\pm0.8	8.3\pm1.5	
ATLAS-C	SAM-FT	70.1 \pm 2.9	7.2 \pm 1.2	9.1 \pm 1.5	15.3 \pm 2.4	
	SAM+FIP	72.3 \pm 2.5*	6.5 \pm 1.0*	8.0 \pm 1.3*	12.7 \pm 2.1*	Motion artifacts
	SAM+CMP	71.8 \pm 2.3*	6.9 \pm 1.1	7.1 \pm 1.1*	13.2 \pm 2.2*	
	CalSAM	73.4\pm2.0	5.5\pm0.9	6.0\pm1.0	9.6\pm1.7	
BraTS (Orig)	SAM-FT	82.4 \pm 1.2	5.2 \pm 0.9	8.6 \pm 1.2	12.3 \pm 2.1	
	SAM+FIP	83.1 \pm 0.9*	4.9 \pm 0.7*	7.9 \pm 1.1	9.8 \pm 1.7*	Original validation
	SAM+CMP	83.5 \pm 1.0*	5.1 \pm 0.8	6.8 \pm 0.9*	10.2 \pm 1.5*	
	CalSAM	84.7\pm0.8	4.5\pm0.6	6.2\pm0.7	7.4\pm1.2	

Table 3. Comprehensive analysis of calibration performance across methods and datasets. Post-hoc calibration methods (TS, DS) are applied to the SAM-FT model. **Bold** indicates best performance. Lower values are better for all metrics.

Dataset	Method	ECE (\downarrow %)	Brier Score (\downarrow)	ACE (\downarrow %)
BraTS (GE)	SAM-FT (Base)	8.6 \pm 1.3	0.182 \pm 0.020	8.9 \pm 1.4
	+ Focal Loss	7.8 \pm 1.2	0.173 \pm 0.019	8.1 \pm 1.3
	+ Dice++	7.5 \pm 1.1	0.168 \pm 0.018	7.7 \pm 1.2
	+ Temp. Scaling (TS)	7.1 \pm 1.1	0.162 \pm 0.018	7.3 \pm 1.1
	+ Dirichlet (DS)	6.9 \pm 1.0	0.159 \pm 0.017	7.0 \pm 1.1
	CalSAM	5.2 \pm 0.8	0.121 \pm 0.010	5.4 \pm 0.9
ATLAS-C	SAM-FT (Base)	9.1 \pm 1.5	0.195 \pm 0.025	9.4 \pm 1.6
	+ Focal Loss	8.3 \pm 1.4	0.185 \pm 0.024	8.6 \pm 1.5
	+ Dice++	7.9 \pm 1.3	0.179 \pm 0.023	8.1 \pm 1.4
	+ Temp. Scaling (TS)	7.4 \pm 1.2	0.174 \pm 0.022	7.6 \pm 1.3
	+ Dirichlet (DS)	7.2 \pm 1.2	0.171 \pm 0.022	7.3 \pm 1.2
	CalSAM	5.8 \pm 0.9	0.138 \pm 0.015	6.0 \pm 1.0
BraTS (Orig)	SAM-FT (Base)	8.6 \pm 1.2	0.175 \pm 0.018	8.8 \pm 1.3
	+ Focal Loss	7.9 \pm 1.1	0.168 \pm 0.017	8.1 \pm 1.2
	+ Dice++	7.6 \pm 1.0	0.164 \pm 0.016	7.8 \pm 1.1
	+ Temp. Scaling (TS)	7.0 \pm 1.0	0.158 \pm 0.016	7.2 \pm 1.0
	+ Dirichlet (DS)	6.8 \pm 1.0	0.155 \pm 0.016	6.9 \pm 1.0
	CalSAM	6.2 \pm 0.9	0.132 \pm 0.012	6.4 \pm 0.9

by consistently reducing the Expected Calibration Error (ECE). On **BraTS (Orig)**, CalSAM achieves an ECE of $6.2 \pm 0.9\%$, a 28% relative reduction compared to SAM-FT ($8.6 \pm 1.2\%$).

This gain arises from the proposed CMP, which penalizes overconfident false predictions (e.g., false positives in edema regions). Additionally, Fisher information regularization stabilizes feature representations across scanners, mitigating overfitting to site-specific artifacts.

Under the per-center holdout setting (**BraTS GE**), CalSAM achieves the lowest calibration error ($5.2 \pm 0.8\%$) and smallest domain gap (6.8), while also providing an av-

erage Dice improvement of +3.8% over baselines. Similarly, under synthetic corruptions on **ATLAS-C**, CalSAM maintains robustness with the best ECE ($5.8 \pm 0.9\%$), underscoring its consistent calibration performance across diverse domain shifts.

5.1. Ablation Study

We assess the individual contributions of the Fisher Information Penalty (FIP) and the Confidence Misalignment Penalty (CMP). Results are reported in Table 2, averaged over 5 independent runs with mean \pm standard deviation. Statistical significance is evaluated using paired *t*-tests

against the strongest baseline ($p < 0.01$).

FIP improves robustness. Across all domain-shift conditions, incorporating FIP consistently improves Dice and boundary accuracy relative to SAM-FT. On BraTS (Orig), DSC increases from 82.4 ± 1.2 to 83.1 ± 0.9 and HD95 decreases from 5.2 ± 0.9 mm to 4.9 ± 0.7 mm. More importantly, FIP reduces the domain generalization gap (DGG) from 12.3 ± 2.1 to 9.8 ± 1.7 , a 20.3% relative decrease, confirming its role in stabilizing encoder representations under cross-site shifts, consistent with prior findings on Fisher regularization [13].

CMP improves calibration. CMP primarily benefits probabilistic calibration. On BraTS (Orig), ECE decreases from $8.6 \pm 1.2\%$ to $6.8 \pm 0.9\%$, a 21% relative improvement. The gains are even more pronounced on ATLAS-C stroke data, where sharper lesion boundaries yield reductions from $9.1 \pm 1.5\%$ to $7.1 \pm 1.1\%$. CMP also contributes moderate improvements in DSC (e.g., $82.4 \pm 1.2 \rightarrow 83.5 \pm 1.0$), highlighting that calibration gains do not come at the expense of accuracy.

Joint effect in CalSAM. Combining FIP and CMP yields complementary benefits, with CalSAM achieving the best performance across all datasets. On BraTS (GE), CalSAM reaches 77.9 ± 1.5 DSC, 4.8 ± 0.7 mm HD95, and $5.4 \pm 0.8\%$ ECE, outperforming both single-component variants. Similar trends hold for ATLAS-C and BraTS (Orig), establishing CalSAM as both robust and well-calibrated under domain shift.

Calibration baselines. Table 3 reports calibration performance (mean \pm std over 5 runs) for loss-based baselines (Focal Loss, Dice++), post-hoc methods (Temperature/Dirichlet scaling), and CalSAM. Lower is better for all metrics.

Loss-based methods provide modest gains over SAM-FT, post-hoc methods yield larger improvements, and CalSAM consistently outperforms all alternatives.

BraTS (GE). CalSAM reduces ECE to $5.2 \pm 0.8\%$, a 39.5% drop vs. SAM-FT ($8.6 \pm 1.3\%$) and 24.6% vs. Dirichlet ($6.9 \pm 1.0\%$). The Brier score improves to 0.121 ± 0.010 (33.5% vs. SAM-FT, 23.9% vs. Dirichlet). ACE falls to $5.4 \pm 0.9\%$ (39.3% vs. SAM-FT, 22.9% vs. Dirichlet).

ATLAS-C. On motion-corrupted stroke data, CalSAM achieves ECE $5.8 \pm 0.9\%$ (36.3% vs. SAM-FT $9.1 \pm 1.5\%$, 19.4% vs. Dirichlet $7.2 \pm 1.2\%$). Brier decreases to 0.138 ± 0.015 (29.2% vs. SAM-FT, 19.3% vs. Dirichlet). ACE drops to $6.0 \pm 1.0\%$ (36.2% vs. SAM-FT, 17.8% vs. Dirichlet).

BraTS (Orig). ECE improves to $6.2 \pm 0.9\%$ (27.9% vs. SAM-FT $8.6 \pm 1.2\%$, 8.8% vs. Dirichlet $6.8 \pm 1.0\%$). Brier reaches 0.132 ± 0.012 (24.6% vs. SAM-FT, 14.8% vs. Dirichlet). ACE is $6.4 \pm 0.9\%$ (27.3% vs. SAM-FT, 7.2% vs. Dirichlet).

In summary, post-hoc methods, especially Dirichlet scaling, substantially improve calibration over SAM-FT. CalSAM delivers the largest gains across datasets and metrics (typically 20–40% vs. SAM-FT and 8–25% vs. the best baseline), demonstrating the benefit of joint robustness and calibration training under domain shift.

Limitation. Fisher information penalty increases training time by 15% due to second-order gradient calculations.

Conclusion

We presented **CalSAM**, a confidence-calibrated adaptation method that jointly addresses covariate shift and over-confident segmentation outputs when applying SAM to brain MRI. CalSAM combines a 3D-aware Fisher information penalty (FIP) to stabilize feature sensitivity with a confidence misalignment penalty (CMP) to suppress high-confidence errors; the combined training objective fine-tunes only SAM’s mask decoder. Empirically, CalSAM reduces domain generalization gaps and calibration errors while improving Dice and boundary accuracy across BraTS and ATLAS benchmarks. For example, on the BraTS scanner-split CalSAM achieves DSC = $80.1 \pm 1.3\%$ and ECE = $5.2 \pm 0.8\%$, while on ATLAS-C it yields DSC = $75.9 \pm 2.0\%$. Ablation experiments confirm the complementary roles of FIP and CMP, with statistically significant improvements over single-component variants. We also highlight a practical limitation: FIP’s second-order gradient computations increase training time by about 15%. Theoretical analysis (Proposition 2.1 and Corollary 2.1) further connects Fisher control to tighter generalization and calibration bounds under covariate shift. In summary, CalSAM is a practicable step toward deploying foundation segmentation models in clinical imaging by jointly improving accuracy and uncertainty under realistic domain shifts. Code and containerized environments will be released to foster reproducibility at anonymous link [CalSAM](#).

References

- [1] Ana Barragán-Montero, Adrien Bibal, Margerie Huet Das tarac, Camille Draguet, Gilmer Valdes, Dan Nguyen, Siri Willems, Liesbeth Vandewincke, Mats Holmström, Fredrik Löfman, et al. Towards a safe and efficient clinical implementation of machine learning in radiation oncology by exploring model interpretability, explainability and data-model dependency. *Physics in Medicine & Biology*, 67(11): 11TR01, 2022. 4
- [2] Andreas Bennström and Filip Winzell. Automated 3d bone

segmentation using deep learning in scoliosis. *Master's Thesis in Mathematical Sciences*, 2021. 4

[3] M Jorge Cardoso, Wenqi Li, Richard Brown, Nic Ma, Eric Kerfoot, Yiheng Wang, Benjamin Murrey, Andriy Myronenko, Can Zhao, Dong Yang, et al. Monai: An open-source framework for deep learning in healthcare. *arXiv preprint arXiv:2211.02701*, 2022. 5

[4] Haotian Chen, Yonghui Xu, Yanyu Xu, Yixin Zhang, and Lizhen Cui. Test-time medical image segmentation using clip-guided sam adaptation. In *2024 IEEE International Conference on Bioinformatics and Biomedicine (BIBM)*, pages 1866–1873. IEEE, 2024. 4

[5] John Duchi. Distributional robustness, regularizing variance, and adversaries. *arXiv*, 2017. 4

[6] Gintare Karolina Dziugaite and Daniel M Roy. Data-dependent pac-bayes priors via differential privacy. *Advances in neural information processing systems*, 31, 2018. 3, 4

[7] Chuan Guo, Geoff Pleiss, Yu Sun, and Kilian Q Weinberger. On calibration of modern neural networks. In *International conference on machine learning*, pages 1321–1330. PMLR, 2017. 4

[8] Yuhao Huang, Xin Yang, Lian Liu, Han Zhou, Ao Chang, Xinrui Zhou, Rusi Chen, Junxuan Yu, Jiongquan Chen, Chaoyu Chen, et al. Segment anything model for medical images? *Medical Image Analysis*, 92:103061, 2024. 1, 4

[9] Fabian Isensee, Paul F Jaeger, Simon AA Kohl, Jens Petersen, and Klaus H Maier-Hein. nnu-net: a self-configuring method for deep learning-based biomedical image segmentation. *Nature methods*, 18(2):203–211, 2021. 1

[10] Alain Jungo and Mauricio Reyes. Assessing reliability and challenges of uncertainty estimations for medical image segmentation. In *Medical Image Computing and Computer Assisted Intervention–MICCAI 2019: 22nd International Conference, Shenzhen, China, October 13–17, 2019, Proceedings, Part II* 22, pages 48–56. Springer, 2019. 4

[11] Konstantinos Kamnitsas, Christian Baumgartner, Christian Ledig, Virginia Newcombe, Joanna Simpson, Andrew Kane, David Menon, Aditya Nori, Antonio Criminisi, Daniel Rueckert, et al. Unsupervised domain adaptation in brain lesion segmentation with adversarial networks. In *Information Processing in Medical Imaging: 25th International Conference, IPMI 2017, Boone, NC, USA, June 25–30, 2017, Proceedings* 25, pages 597–609. Springer, 2017. 4

[12] Behraj Khan, Rizwan Qureshi, Nouman Muhammad Durra, and Tahir Qasim Syed. Confidence-calibrated covariate shift correction for few-shot classification in vision-language models. In *Proceedings of the Computer Vision and Pattern Recognition Conference*, pages 6511–6523, 2025. 1, 2, 4

[13] Minyoung Kim, Da Li, Shell X Hu, and Timothy Hospedales. Fisher sam: Information geometry and sharpness aware minimisation. In *International Conference on Machine Learning*, pages 11148–11161. PMLR, 2022. 4, 8

[14] Alexander Kirillov, Eric Mintun, Nikhila Ravi, Hanzi Mao, Chloe Rolland, Laura Gustafson, Tete Xiao, Spencer Whitehead, Alexander C Berg, Wan-Yen Lo, et al. Segment anything. In *Proceedings of the IEEE/CVF international conference on computer vision*, pages 4015–4026, 2023. 1, 6

[15] Simon Kohl, Bernardino Romera-Paredes, Clemens Meyer, Jeffrey De Fauw, Joseph R Ledsam, Klaus Maier-Hein, SM Eslami, Danilo Jimenez Rezende, and Olaf Ronneberger. A probabilistic u-net for segmentation of ambiguous images. *Advances in neural information processing systems*, 31, 2018. 4

[16] Meelis Kull, Miquel Perello Nieto, Markus Kängsepp, Telmo Silva Filho, Hao Song, and Peter Flach. Beyond temperature scaling: Obtaining well-calibrated multi-class probabilities with dirichlet calibration. *Advances in neural information processing systems*, 32, 2019. 4

[17] Ananya Kumar, Percy S Liang, and Tengyu Ma. Verified uncertainty calibration. *Advances in neural information processing systems*, 32, 2019. 4

[18] Frederik Kunstner, Philipp Hennig, and Lukas Balles. Limitations of the empirical fisher approximation for natural gradient descent. *Advances in neural information processing systems*, 32, 2019. 5

[19] Yann LeCun, Léon Bottou, Genevieve B Orr, and Klaus-Robert Müller. Efficient backprop. In *Neural networks: Tricks of the trade*, pages 9–50. Springer, 2002. 3

[20] Sook-Lei Liew, Bethany P Lo, Miranda R Donnelly, Artemis Zavaliangos-Petropulu, Jessica N Jeong, Giuseppe Barisano, Alexandre Hutton, Julia P Simon, Julia M Juliano, Anisha Suri, et al. A large, curated, open-source stroke neuroimaging dataset to improve lesion segmentation algorithms. *Scientific data*, 9(1):320, 2022. 4

[21] Jun Ma, Yuting He, Feifei Li, Lin Han, Chenyu You, and Bo Wang. Segment anything in medical images. *Nature Communications*, 15(1):654, 2024. 1, 4, 6

[22] Oskar Maier, Bjoern H Menze, Janina Von der Gablentz, Levin Häni, Matthias P Heinrich, Matthias Liebrand, Stefan Winzeck, Abdul Basit, Paul Bentley, Liang Chen, et al. Isles 2015-a public evaluation benchmark for ischemic stroke lesion segmentation from multispectral mri. *Medical image analysis*, 35:250–269, 2017. 4

[23] David A. McAllester. Pac-bayesian model averaging. In *Proceedings of the twelfth annual conference on Computational learning theory*, pages 164–170. ACM, 1999. 3, 4

[24] Bjoern H Menze, Andras Jakab, Stefan Bauer, Jayashree Kalpathy-Cramer, Keyvan Farahani, Justin Kirby, Yuliya Burren, Nicole Porz, Johannes Slotboom, Roland Wiest, et al. The multimodal brain tumor image segmentation benchmark (brats). *IEEE transactions on medical imaging*, 34(10):1993–2024, 2014. 4

[25] Maxime Oquab, Timothée Darct, Théo Moutakanni, Huy Vo, Marc Szafraniec, Vasil Khalidov, Pierre Fernandez, Daniel Haziza, Francisco Massa, Alaaeldin El-Nouby, et al. Dinov2: Learning robust visual features without supervision. *arXiv preprint arXiv:2304.07193*, 2023. 1

[26] Olaf Ronneberger, Philipp Fischer, and Thomas Brox. U-net: Convolutional networks for biomedical image segmentation. In *Medical image computing and computer-assisted intervention–MICCAI 2015: 18th international conference, Munich, Germany, October 5–9, 2015, proceedings, part III* 18, pages 234–241. Springer, 2015. 1

[27] Alexander Soen and Ke Sun. On the variance of the fisher

information for deep learning. *Advances in Neural Information Processing Systems*, 34:5708–5719, 2021. 3

[28] Masashi Sugiyama, Matthias Krauledat, and Klaus-Robert Müller. Covariate shift adaptation by importance weighted cross validation. *Journal of Machine Learning Research*, 8 (5), 2007. 2

[29] Hongqiu Wang, Jian Chen, Shichen Zhang, Yuan He, Jinfeng Xu, Mengwan Wu, Jinlan He, Wenjun Liao, and Xiangde Luo. Dual-reference source-free active domain adaptation for nasopharyngeal carcinoma tumor segmentation across multiple hospitals. *IEEE Transactions on Medical Imaging*, 2024. 1, 4

[30] Michael Yeung, Leonardo Rundo, Yang Nan, Evis Sala, Carola-Bibiane Schönlieb, and Guang Yang. Calibrating the dice loss to handle neural network overconfidence for biomedical image segmentation. *Journal of Digital Imaging*, 36(2):739–752, 2023. 4

[31] Kihyun You, Jawook Gu, Jiyeon Ham, Beomhee Park, Jiho Kim, Eun K Hong, Woonhyuk Baek, and Byungseok Roh. Cxr-clip: Toward large scale chest x-ray language-image pre-training. In *International Conference on Medical Image Computing and Computer-Assisted Intervention*, pages 101–111. Springer, 2023. 1

[32] Feiyang Yu, Alex Moehrung, Oishi Banerjee, Tobias Salz, Nikhil Agarwal, and Pranav Rajpurkar. Heterogeneity and predictors of the effects of ai assistance on radiologists. *Nature Medicine*, 30(3):837–849, 2024. 1

[33] Jianpeng Zhang, Yutong Xie, Yong Xia, and Chunhua Shen. Dodnet: Learning to segment multi-organ and tumors from multiple partially labeled datasets. In *Proceedings of the IEEE/CVF conference on computer vision and pattern recognition*, pages 1195–1204, 2021. 4

[34] Qin Zhang, Linghan Xu, Qingming Tang, Jun Fang, Ying Nian Wu, Joe Tighe, and Yifan Xing. Threshold-consistent margin loss for open-world deep metric learning. *arXiv preprint arXiv:2307.04047*, 2023. 4

[35] Sheng Zhang, Yanbo Xu, Naoto Usuyama, Hanwen Xu, Jaspreet Bagga, Robert Tinn, Sam Preston, Rajesh Rao, Mu Wei, Naveen Valluri, et al. Biomedclip: a multimodal biomedical foundation model pretrained from fifteen million scientific image-text pairs. *arXiv preprint arXiv:2303.00915*, 2023. 1